Exploiting Surface Water on Carbon Aerogels for Ultra-Sensitive and Selective NO_2 Gas Detection

Sebastian Nufer[1,2,*], Peter J. Lynch[2], Matthew J. Large[2], Sean P. Ogilvie[2], Jonathan P. Salvage[3], Mario Pelaez-Fernandez[4], Edgar Muñoz[5], Raul Arenal[4,6,7], Ana M. Benito[5], Wolfgang K. Maser[5], Nikos Tagmatarchis[8], Chris Ewels[9,*], Adam Brunton[1], Alan B. Dalton[2,*]

1 M-Solv Ltd, Oxonian Park, Langford Locks, Kidlington, Oxford, OX5 1FP, UK, Sebastian.Nufer@m-solv.com

2 University of Sussex, Department of Physics and Astronomy, Brighton, BN1 9RH, UK, A.B.Dalton@sussex.ac.uk

3 University of Brighton, School of Pharmacy and Biomolecular Science, Brighton, BN2 4GJ, UK

4 Instituto de Nanociencia de Aragon, Universidad de Zaragoza, Laboratorio de Microscopias Avanzadas (LMA), 50018 Zaragoza, Spain

5 Instituto de Carboquímica ICB-CSIC, 50018 Zaragoza, Spain

6 Fundacion ARAID, 50018 Zaragoza, Spain

7 Instituto de Ciencias de Materiales de Aragon, CSIC-Universidad de Zaragoza, 50009 Zaragoza, Spain

8 Theoretical and Physical Chemistry Institute, National Hellenic Research Foundation, 48 Vassileos Constantinou Avenue, 11635 Athens, Greece

9 Institute des Matériaux Jean Rouxel (IMN), CNRS UMR6502 / Université de Nantes, Nantes, 44322, France, Chris.Ewels@cnrs-imn.fr

[Abstract]

Moisture layers are universally present on nanomaterial surfaces in ambient conditions but rarely acknowledged. Here we actively exploit such layers to produce a cheap carbon aerogel gas sensor, selective to NO_2 compared to ammonia and other volatile organic compounds, that detects at concentrations of at least 10 parts-per-billion. A one step synthesis involving laser deposition and annealing results in a thin soot-like aerogel film of carbon clusters. Surface moisture forms a percolative network on this porous scaffold, whose conductivity varies drastically with ion concentration. The new sensing mechanism, based on the solubility of NO_2 in the water layer, mirrors atmospheric soot chemistry and facilitates the usability of the sensor in practically-relevant ambient environments. The low cost and scalable production shows promise for Internet-of-Things air quality monitoring. More generally this result demonstrates the potential for exploitation of surface water layers on nanoscale scaffolds for applications including sensing, energy capture and storage.

Keywords: Nitrogen dioxide, gas sensor, carbon aerogel, selective, chemiresistor

Surface water is an "elephant in the room" in nanoscience: universally present and yet commonly ignored. It is generally unavoidable, and must be taken into account in any ambient surface-based nanophysics and nanochemistry. Nonetheless its presence and effects are rarely commented on, despite extensive literature in related disciplines such as environmental science. In the current study we show that such surface water can be successfully exploited, here for a low-cost chemiresistor gas sensor that is both highly sensitive and selective. In order to maximise available surface we use carbon aerogels. Laser deposited carbon aerogel (LDCA) is an amorphous carbon nanomaterial formed in a diffusion-limited aggregation process when a focused laser beam interacts with a carbon target.[1,2] Carbon clusters are produced in the plasma formed above the target which

subsequently diffuse to a second substrate where they aggregate, similar to the concept of pulsed laser deposition.[2–4] The resulting aggregates form conductive dendritic structures with nanometre-scale features and low density, whose surface oxygen content renders them hydrophilic. This combination of porosity and high specific surface area in a conductive thin film makes LDCA a promising material for high-sensitivity gas sensing and other applications.[2,5]

Nitrogen dioxide (NO_2) poses a substantial health risk causing respiratory issues which are particularly severe for asthma sufferers[6] and infants.[7] European Union regulations allow a threshold of 20 parts-per-billion (ppb) of NO_2 in the air to be overcome not more than 18 times in a year,[8] yet in London alone the monthly average regularly exceeds this.[9] Monitoring air quality at ppb levels currently requires unwieldy, expensive equipment and is therefore scarcely implemented[10,11] and as such, a major challenge centres on the development of highly sensitive, accurate and low-cost devices for widespread continuous monitoring of NO_2 levels in domestic, public and industrial environments. Metal oxides are well established as commercially-available gas sensors capable of selectively detecting NO_2 at concentrations down to 10 ppb,[12] however they normally operate at elevated temperatures resulting in increased power consumption and limiting use in small scale measurement configurations and devices. Nanomaterial structures, many carbon based, have emerged in the last decade which facilitate detection of gases at low concentration with thousand fold reduction in power consumption over metal oxides.[13] However, while candidates such as graphene and carbon nanotubes exhibit low detection limits they are not chemically selective in their pristine form.[9,13,14] Functionalization can overcome this but adds a complicated step during fabrication, increasing costs.[15,16]

Here, we present a cheap, selective NO_2 sensing layer based on a LDCA with excellent limit of detection (<10 ppb) produced by a scalable one-step laser deposition process, which we incorporate into a chemiresistor device. The device and sensing layer are characterised via scanning electron microscopy (SEM), X-ray photoelectron spectroscopy (XPS), Raman spectroscopy, and cyclic voltammetry. Sensitivity and detection limits are determined, and several volatile organic compounds (VOCs) are used to ascertain the selectivity, while measurements in different background environments establish the sensing mechanism and origin of the selectivity. We show that this depends on the solubility and the reaction of the analyte with the water layer formed on the LDCA, which connects non-percolating graphitic regions, mirroring behaviour seen in atmospheric soot chemistry.[17–20]

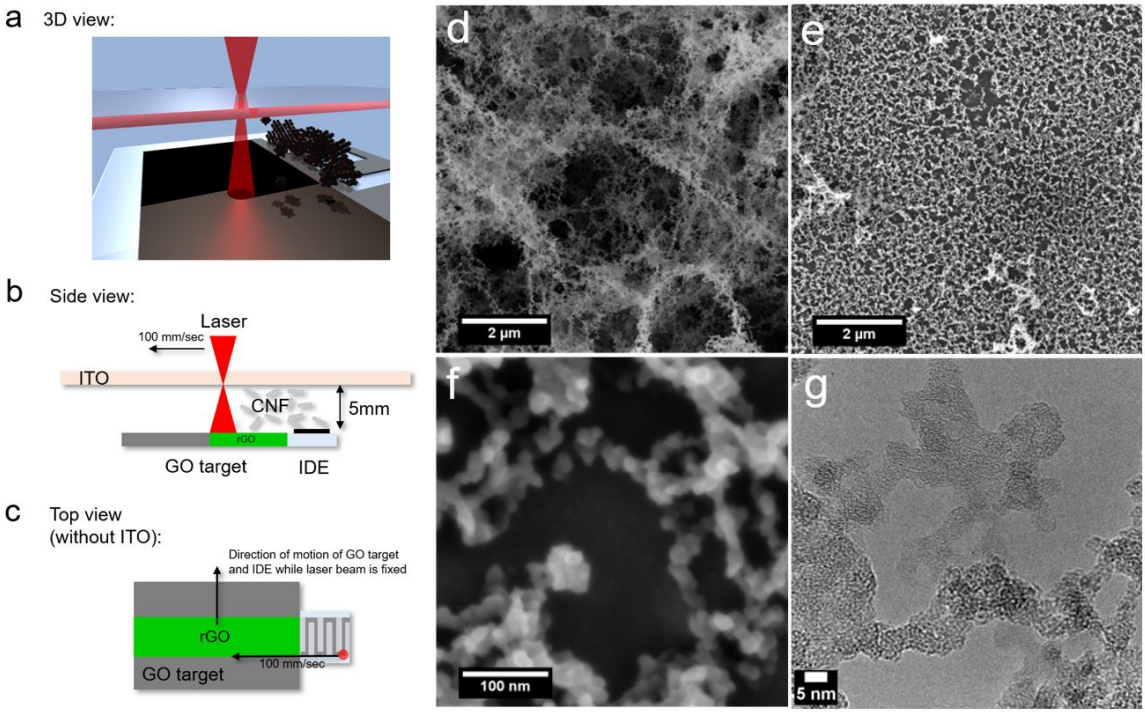

Figure 1 a) Fabrication setup in 3D, b) side and c) top view of processing steps of the fabrication. SEM image of d) carbon aerogel diffusion barrier, e) active layer after removal of diffusion barrier, f) high magnification image of active layer, showing individual carbon clusters, g) HRTEM of LDCA diffusion barrier layer

The deposition process is depicted in **Figure 1** and further detailed in **Figure S1**. Interdigitated electrodes (IDE), formed by laser ablation, are placed next to a target which

acts as a carbon source. Graphene oxide (GO) prepared by drop casting on a borosilicate glass slide was used as the pre-cursor material (see supplementary information). A transparent hydrophobic material, in our case indium tin oxide (ITO) sputtered on glass, is held above the target and substrate with a small airgap in between. Using previously optimised conditions, an infrared laser with a constant fluence of 417 mJ/cm^2 is focused onto the ITO.[2] The laser ablates a line into the ITO allowing the laser light to interact with the GO target below. The laser is then scanned across both the GO target and the IDE substrate. As the laser interacts with the GO target, it produces reduced graphene oxide (rGO)[2] as well as a plume of carbon and oxygen atoms. These rapidly form clusters which diffuse toward the IDE substrate. This diffusion is partially directed by the ITO layer to which the clusters do not to adhere due to its hydrophobic nature.

Simultaneously, the target and IDE substrate are moved perpendicularly to the laser scan direction, feeding un-processed GO to the LDCA deposition process and eventually covering the whole IDE area with deposited material (see **Figure S1d**). The laser also moves over the IDE substrate with each pass, irradiating and annealing the already deposited LDCA and improving its substrate adhesion markedly. It is this annealed LDCA that forms the active sensor layer. As the process proceeds, excess material may overcoat the active layer acting as a diffusion barrier to analytes. To maximise device performance this is therefore subsequently removed by blowing pressurised air over the device once prepared (see **Figure S1e**).

Figure 1d-g details the various stages of LDCA preparation. **Figure S5** shows the IDEs made with a laser ablation process from molybdenum coated glass. **Figure 1d** shows the as-deposited LDCA formed on top of the laser-annealed active layer. The active layer has a uniform porous structure, significantly denser than the as-prepared material (**Figure 1e**), while higher magnification reveals the assembled carbon aggregates, where the cluster size is

approximately 20 nm (**Figure 1f**). **Figure 1g** and **S6** show HRTEM images of the LDCA consisting of individual particulates in a non-crystalline mesostructure.

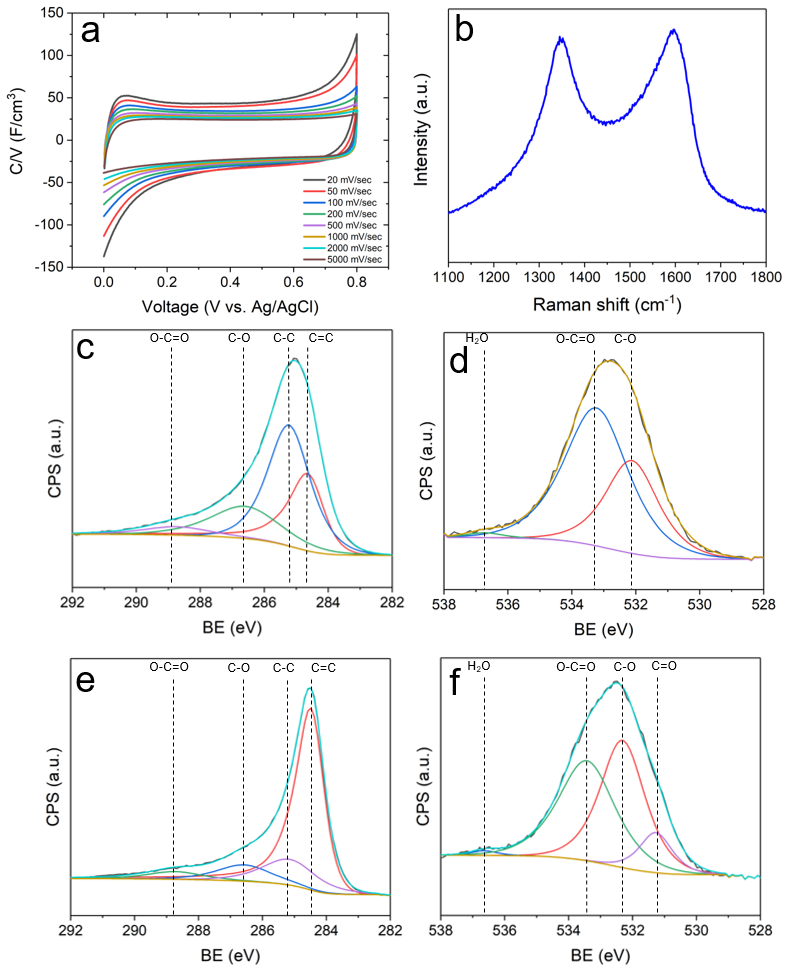

Figure 2 a) Cyclic voltamographs at different cycling rates of active LDCA layer, b) Raman of annealed active LDCA layer c) Deconvoluted XPS spectra of C1-peak of diffusion barrier layer, d) Deconvoluted XPS spectra of O-peak of diffusion barrier layer, e) Deconvoluted XPS spectra of C1-peak of active LDCA layer f) Deconvoluted XPS spectra of O-peak of active LDCA layer

To characterise the available surface area within the active LDCA the double layer capacitance was probed using cyclic voltammetry. The cyclic voltamographs (**Figure 2a**) show Faradaic reactions at the extrema with flat central regions, characteristic of non-Faradic double layer electrochemistry. As the scan rate increases these extrema decrease to show a more symmetrical, box-like voltamograph characteristic of a super-capacitor. At low scan rates the double layer capacitance is approximately 45 F/cm^3, corresponding to an internal surface area per unit volume of $2.25 \cdot 10^6$ cm^2/cm^3 assuming a 20 μF/cm^2 theoretical

capacitance for sp^2-hybridized carbon.[21] Interestingly, this is appreciably higher than soot or carbon black which can be up to 10^5 cm^2/cm^3. [22] The layer thickness was estimated using an ellipsometer to be around 100 nm.

Raman spectra (shown in **Figure 2b**) have characteristic D and G peaks, corresponding to defect and lattice modes respectively, with approximately equal intensity indicative of amorphous carbon.[23] XPS allows quantitative chemical analysis of the composition of the as-deposited and annealed LDCA material. **Figure 2e** indicates a high sp^2:sp^3 ratio for the annealed LDCA (around 62 at.% sp^2), greater than that for the as-deposited LDCA (around 22 at.% sp^2), shown in **Figure 2c**, despite their comparable C/O ratio of around 5. In addition, the presence of oxygen functional groups and adsorbed water on the surface is reduced after annealing (**Figure 2f**), suggesting some functionalisation of the surface despite the increase in sp^2 character. Together, these measurements indicate that annealed LDCA comprises significant sp^2 carbon domains contained within functionalised shells.

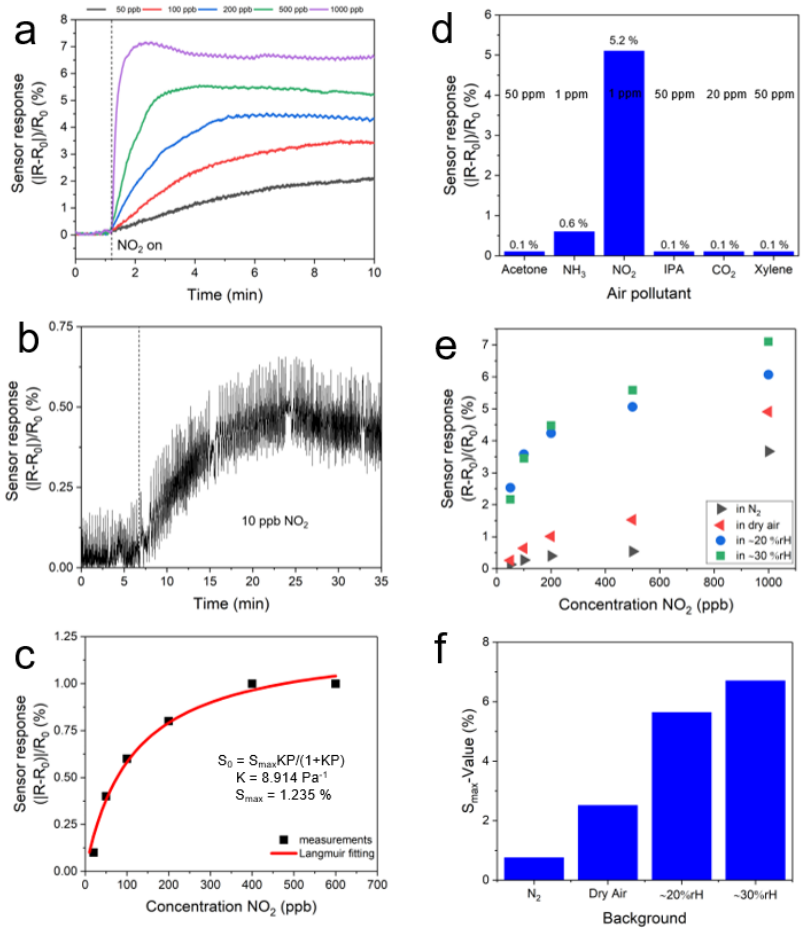

Figure 3 a) Exposure to various concentrations from 50 ppb to 1000 ppb NO_2 in 30%rH air, b) single exposure to 10 ppb NO_2 in dry air, c) calibration curve with a Langmuir fitting in dry air showing surface adsorption behaviour, d) selectivity measurements using NO_2, NH_3 and various VOCs, a concentration of 1 ppm of NO_2 (in dry air) and NH_3 (in dry air), a concentration of 20 ppm of CO_2 (in 20% rH) and 50 ppm of acetone, IPA and xylene was used for the measurement (all in 30% rH), e) NO_2 calibration curve measurement in different backgrounds, f) S_{max}-values derived from Langmuir calibration curves fitted to the different background measurements

Figure 3a shows the sensor response to concentrations between 50 ppb and 1 ppm of NO_2 in a 30% relative humidity air environment. The sensor amplitude increases with NO_2 concentration and saturates after an initial rise. **Figure 3b** depicts the measurement of a device exposed to 10 ppb of NO_2 in dry air. A clear step is seen for this ultra-low concentration with adsorption time t_{90}, the time taken to reach 90% of the full amplitude, of around 10 min. **Figure 3c** shows a response curve for the sensor as a function of

concentration of NO_2 in dry air. The observed saturating behaviour can be described using a Langmuir isotherm of the form $S_0 = S_{max}KP/(1+KP)$, where S_0 is the sensor response, S_{max} is a constant, K is the equilibrium constant of the adsorption and desorption, and P is the partial pressure of the analyte. This model assumes surface adsorption/desorption of an analyte, and has been shown to apply well in the case of nanostructured materials.[24] The model is fitted to the data of **Figure 3c** in the low-concentration operating regime and accurately reproduces the observed trend, with a fitting constant S_{max} = 1.235 % and K = 8.914 Pa^{-1}. This calibration curve allows the readout of an exact concentration value. **Figure 3d** shows the response of the sensor towards different analytes at concentrations of 1 ppm of NH_3, 20 ppm of CO_2, 50 ppm of acetone, IPA and xylene respectively. Whereas NO_2 shows a strong response, the signals from NH_3 and other common VOCs are negligible, indicating a very high degree of selectivity towards NO_2. **Figure 3e** shows the operation of the sensor in different background environments, including dry nitrogen, dry air, and at increasing humidity in air. The sensors have an elevated response in the presence of oxygen (dry air compared to N_2) and notably in a humid environment (30 %rH). **Figure 3f** shows the S_{max} values for the different backgrounds showing an increase with increasing humidity. For reference, a single entire gas exposure cycle is depicted in **Figure S7**.

NO_2 detection by nanocarbon materials is commonly described via surface adsorption of gaseous NO_2 giving rise to charge transfer and an associated shift in the Fermi level of conjugated carbon nanomaterial.[25] This shift changes the conductivity,[26] notably in graphene and nanotubes where the density of states near to the Fermi level is very low. NO_2 binding is shown to be stronger in the presence of pre-existing defects in the carbon,[27] such as at nanosheet edges in graphene films[28] or more readily on the surfaces of materials functionalised to improve their sensitivity and/or selectivity.[29] However, such a single mechanism does not account for the strong variation of sensitivity with atmospheric humidity

seen here (**Figure 3e**) even in a situation of competitive adsorption of both analyte and water molecules. We propose instead a new mechanism, shown in **Figure 4a**, closely related to known reactions in soot chemistry.[17–20]

This additional sensing mechanism can be understood based on the structure of the sensing layer (**Figure 1g**). It consists of a low-density array of carbon particles, very reminiscent of oxygen-poor soots (see Supplementary **Figure S8b,c**). The XPS data suggests that after laser irradiation the particle surfaces and intermediate low-conductivity soot are functionalized with oxygen-containing species such as carboxyl groups. The material will therefore be highly hydrophilic and unless carefully excluded through appropriate heating and drying, a surface water layer will be present.

When this network of carbonaceous particles is weakly connected or below a percolation threshold, its overall conductivity will be mediated by conduction through the surface water layer, which acts as a bridge between nearby particles. Thus, material conductivity will be strongly dependent on the conductivity through the water bridges, which in turn will strongly depend on ion content in the water.

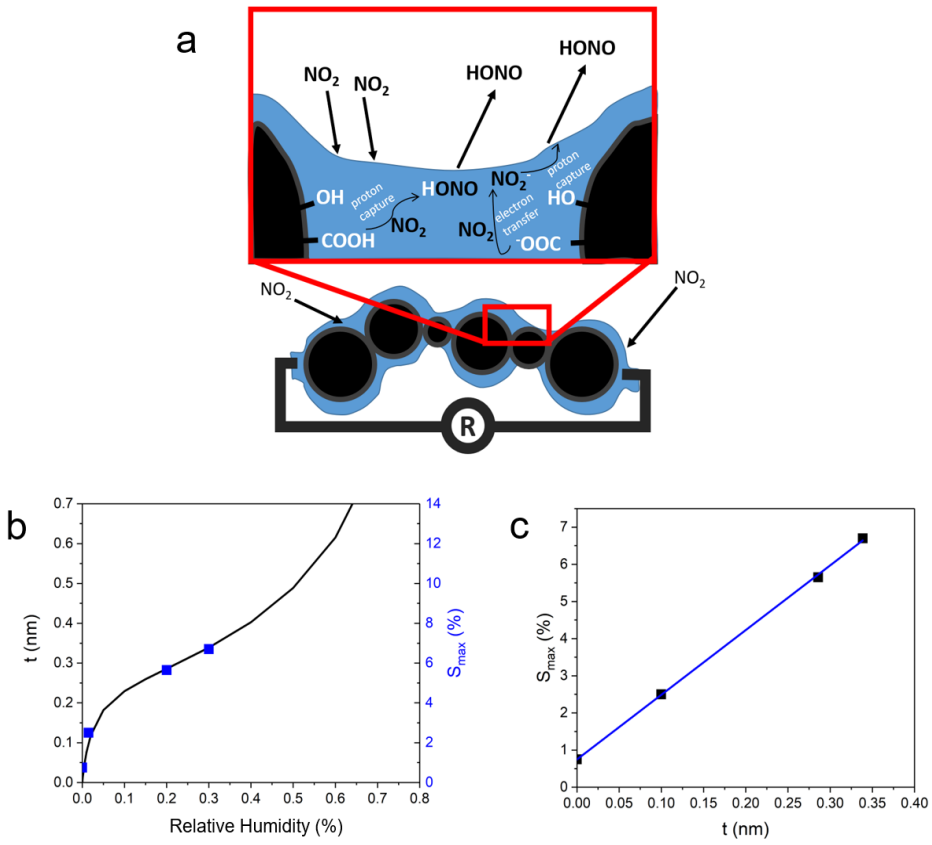

Figure 4 a) Schematic showing the carbon particles with surface water layer and bridging water, with example reactions as NO_2 interacts with the water and organic carbon. R is the external resistance measurement which is primarily governed by the resistance of the water bridging the particles, b) Calculated BET isotherm showing the thickness of the adsorbed water layer against humidity, plotted alongside the sensitivity metric S_{max}, c) Plot of S_{max} vs adsorbed water layer thickness t, illustrating a robust linear trend

As NO_2 dissolves in the water layer, interaction with the carbon surface chemistry results in ion formation in solution.[17,19,30,31] Such reactions are responsible for the selectivity of LDCA for NO_2. While the intrinsic water solubility of NO_2 is low,[30] in the presence of carbonaceous species this changes whereby dissolved NO_2 reacts with soot particles to form nitrous acid HONO.[19] These acid species result in soluble ions such as NO_2^- and NO_4^- and can result in significant NO_2 take-up.[17] The gas sensor is thus measuring, via resistance change, the ion concentration in the electrode surface water layer, and indirectly therefore, the NO_2 breakdown process of the carbon layer. We note that the importance of the water

layer can be demonstrated by freezing; operating at -25C decreases the sensor response to 1ppm NO_2 by an order of magnitude as compared to room temperature.

As mentioned above, oxidised soot particles are also known to have carboxylated surfaces[32] which can interact strongly with water vapour,[33] notably in atmospheric chemistry where they can act as cloud nuclei.[32] We tested the above theory through production of a similar sensor fabricated using propane soot, which indeed also shows NO_2 detection, albeit at lower sensitivity (presumably due to less optimal structure and porosity, see **Figure S9**). We note that this mechanism also explains why there is higher sensitivity to NO_2 than NH_3. While NH_3 has extremely high water solubility, it will rapidly form ionic dielectric shells around opposing exposed carbon surfaces in the electrode, and hence, while there will be a strong initial capacitive response, there is no subsequent electrolytic response or mechanism for continuous ion transfer.[34] In contrast conduction with NO_2 is mediated through continuous reaction with the carbonaceous electrode.

To understand the apparent increasing sensitivity (indicated by the value of S_{max}) as a function of humidity, we use the BET isotherm (calculation outlined in Supplementary Note 5) to evaluate the changing thickness of the adsorbed water layer on the LDCA. **Figure 4b** compares the resulting calculated water layer thickness with the fitted S_{max} values as a function of relative humidity and points to a clear correlation between the two. This correlation is further evidenced in **Figure 4c** where S_{max} is plotted as a function of water layer thickness and fitted to a simple linear regression. Interestingly, the intercept of regression is non-zero. Clearly, there is both sensitivity at zero humidity (corresponding to the sensor measurements performed in dry nitrogen) and an increase in sensitivity with adsorbed thickness of the water layer lending support to the hypothesised mechanism based on

dissolution of NO_2 within the adsorbed water layer. We note that if dissolution within the water layer was solely responsible for the sensing response, we should expect there to be no analyte response in the absence of an adsorbed water layer. Although the presence of pre-existing chemisorbed water cannot be discounted, this may infer that, at very low values of humidity, there is potentially a second sensing mechanism contributing to the overall sensor response based on direct adsorption of NO_2.[35]

This mechanism presented accounts for the sensitivity, selectivity and humidity dependence of this LDCA gas sensor, justifying its impressive performance and potential to compete with existing room-temperature NO_2 sensing materials.

In summary, a thin, porous and well adhered film of LDCA is deposited in a cheap but scalable single-step laser process on readout electrodes to form a chemiresistor structure for distributed air quality monitoring. Exposure to NO_2 shows a detection limit below 10 ppb and rapid response times below 15 min, facilitating simple measurements of NO_2 pollution in air in compliance with EU regulations. These as-produced LDCA sensors show exceptional selectivity towards NO_2 over other common air pollutants making them unique amongst carbon nanomaterials,[9,13,29,36–39] performing better in a humid environment making them readily applicable for real world measurements. Intriguingly while high temperature sensor operation is traditionally used explicitly to avoid surface water contamination,[40] in the current study we demonstrate that surface absorbed water actively mediates the NO_2 sensing. A novel sensing mechanism is identified exploiting NO_2 solubility and reactivity in a percolative network of surface water, mirroring reactions seen in environmental atmospheric chemistry. Surface liquids on high surface area nanoscale scaffolds, often seen as an

unavoidable nuisance, may in fact hold great potential for exploitation in other areas as well as sensing, such as energy capture and storage.

Experimental Section

Device fabrication. For the IDEs the substrate material used was a sputtered thin film of molybdenum on glass purchased from AimCore Technology (Hsinchu 30351, Taiwan). An MSV-101 (M-Solv Ltd, UK) laser-processing platform was used to pattern a 10mm x 10mm interdigitated electrode design into the thin metal film using a galvanoscanner and a pulsed infrared laser (1064 nm, Multiwave, set to 150 kHz repetition rate, 10 ns pulse length) with a fluence of 3 J/cm^2 at a beam scanning speed of 1000 mm/sec. The same platform was then used to deposit the LDCA on to the IDEs. The ITO was held in place with a homemade vacuum holder. The GO was deposited on borosilicate glass using the drop cast method and two iterations to create a thick film. The GO was heated to 250°C in a ramping process of 3°/min starting at room temperature. The Multiwave laser was set to 200 kHz resulting in 417 mJ/cm^2 with a mark-speed of 100 mm/sec. A hand held dry air blower was used to remove the LDCA diffusion barrier.

Material characterisation. Samples were imaged with a Zeiss SIGMA field emission gun scanning electron microscope (FEG-SEM) using a Zeiss in-lens secondary electron detector. The FEG-SEM working conditions used were 2.5 kV accelerating voltage, 20 µm aperture, and 2 mm working distance.

Samples were analysed using a Thermo Scientific K-Alpha XPS instrument equipped with a micro-focused monochromated Al X-ray source. The source was operated at 12 keV and a 400 µm spot size. The analyser operates at a constant analyser energy (CAE) 200 eV for survey scans and 50 eV for detailed scans. Charge neutralization was applied using a combined low energy / ion flood source. The spectra were deconvoluted using CASAXPS

software. The XPS peaks were fitted to GL(70) line shape (a combination of 70% Gaussian and 30% Lorentzian character), after performing a Shirley background subtraction. In the fitting procedure, the FWHM (full width at half maximum) values were fixed at a maximum limit of 1.6 eV for all the peaks except the peaks appearing at the higher energy region that tend to be much broader. Asymmetry for the sp^2 carbon peak was defined as a function LA(α, β, m), where α=0.4 and β=0.38 describe the spread of the tail on each side of the Lorentzian component and the parameter m=70 specifies the width of the Gaussian used to convolute the Lorentzian curve.

HRTEM imaging studies were made using an aberration-corrected FEI Titan High-Base microscope, equipped with a CEOS CETCOR Cs objective lens corrector and working at 80 kV. These works have been developed at low electron doses for avoiding potential damage and limiting charging effects.

Raman measurements were carried out using a Renishaw Invia Microscope. A 532 nm 50 mW continuous wave laser was used at 10% intensity for 10 s to produce the Raman spectrum. A total of 10 accumulations were used to enhance the signal.

Electrochemical measurements were made using a 3 electrode setup connected to a Gamry 600+ potentiostat. The reference electrode used as an Ag/AgCl reference and the counter electrode was a platinum wire. The electrolyte used was a 0.5 M aqueous potassium sulfate solution.

Gas measurements. A home-made gas measurement chamber was used for the measurements (see supplementary information **Figure S10**). Alicat mass flow controllers were used to dilute pre-diluted NO_2 in air and nitrogen to the required concentrations. The NO_2 pre diluted cylinders in air and in nitrogen were purchased from BOC Ltd. A LabJack was used to record the electrical data, with a set current of 1 mA. A small ceramic plate

mounted to the back of the device was used to regulate the device temperature. A bubbler system connected to the mass flow controllers allowed the introduction of humid air into the system. A pre-diluted NH_3 in nitrogen were purchased from BOC Ltd for the exposure to ammonia. A standard calibration gas bottle was purchased for the CO_2 exposure. VOCs were added into the bubbler system and the vapour pressure was used to calculate the concentration the device was exposed to.

Supporting Information

Supporting Information is available from the Wiley Online Library or from the author.

Acknowledgments

We thank M-Solv for supporting this project. ABD thanks the Sussex University strategic development fund. This project has received funding from the European Union's Horizon 2020 research and innovation program under the Marie Sklodowska-Curie Grant agreement No 642742. The HRTEM studies were conducted at the Laboratorio de Microscopias Avanzadas, Universidad de Zaragoza, Spain. R.A. acknowledges support from Spanish MINECO grant MAT2016-79776-P (AEI/FEDER, UE), from the Government of Aragon and the European Social Fund (grant number E13_17R, FEDER, UE) and from the European Union H2020 program "ESTEEM3" (grant number 823717) and "Graphene Flagship" (grant number 785219).

Received: ((will be filled in by the editorial staff))
Revised: ((will be filled in by the editorial staff))
Published online: ((will be filled in by the editorial staff))

References

[1] S. Henley, J. Carey, S. Silva, G. Fuge, M. Ashfold, D. Anglos, *Physical Review B* **2005**, *72*, 205413.

[2] S. Nufer, D. Fantanas, S. P. Ogilvie, M. J. Large, D. J. Winterauer, J. P. Salvage, M. Meloni, A. A. King, P. Schellenberger, A. Shmeliov, others, *ACS Applied Nano Materials* **2018**, *1*, 1828.

[3] A. V. Rode, E. G. Gamaly, B. Luther-Davies, *Applied Physics A: Materials Science & Processing* **2000**, *70*, 135.

[4] A. V. Rode, S. Hyde, E. Gamaly, R. Elliman, D. McKenzie, S. Bulcock, *Applied Physics A: Materials Science & Processing* **1999**, *69*, S755.

[5] S. Nufer, P. Lynch, M. Cann, M. J. Large, J. P. Salvage, S. Victor-Román, J. Hernández-Ferrer, A. M. Benito, W. K. Maser, A. Brunton, others, *ACS Omega* **2018**, *3*, 15134.

[6] J. Orehek, J. P. Massari, P. Gayrard, C. Grimaud, J. Charpin, *J. Clin. Invest.* **1976**, *57*, 301.

[7] I. Aguilera, M. Pedersen, R. Garcia-Esteban, F. Ballester, M. Basterrechea, A. Esplugues, A. Fernández-Somoano, A. Lertxundi, A. Tardón, J. Sunyer, *Environ. Health Perspect.* **2013**, *121*, 387.

[8] E. Agency, *www.gov.uk* **2016**.

[9] C. Melios, V. Panchal, K. Edmonds, A. Lartsev, R. Yakimova, O. Kazakova, *ACS Sensors* **2018**, *3*, 1666.

[10] X. Liu, S. Cheng, H. Liu, S. Hu, D. Zhang, H. Ning, *Sensors* **2012**, *12*, 9635.

[11] J. S. Apte, K. P. Messier, S. Gani, M. Brauer, T. W. Kirchstetter, M. M. Lunden, J. D. Marshall, C. J. Portier, R. C. Vermeulen, S. P. Hamburg, *Environmental Science & Technology* **2017**, *51*, 6999.

[12] Z. Zhang, Z. Wen, Z. Ye, L. Zhu, *Applied Surface Science* **2018**, *434*, 891.

[13] E. Llobet, *Sensors and Actuators B: Chemical* **2013**, *179*, 32.

[14] L. Valentini, I. Armentano, J. Kenny, C. Cantalini, L. Lozzi, S. Santucci, *Applied Physics Letters* **2003**, *82*, 961.

[15] P. Qi, O. Vermesh, M. Grecu, A. Javey, Q. Wang, H. Dai, S. Peng, K. Cho, *Nano Letters* **2003**, *3*, 347.

[16] M. G. Chung, D. H. Kim, H. M. Lee, T. Kim, J. H. Choi, D. Kyun Seo, J.-B. Yoo, S.-H. Hong, T. J. Kang, Y. H. Kim, *Sensors and Actuators B: Chemical* **2012**, *166*, 172.

[17] N. Lahoutifard, M. Ammann, L. Gutzwiller, B. Ervens, C. George, *Atmospheric Chemistry and Physics* **2002**, *2*, 215.

[18] K. Leistner, *Experimental and Modelling Study of Catalytic Diesel Soot Oxidation*, Université Pierre Et Marie Curie-Paris VI, **2012**.

[19] C. Han, Y. Liu, H. He, *Environ. Sci. Technol.* **2013**, *47*, 3174.

[20] M. E. Monge, B. D'Anna, L. Mazri, A. Giroir-Fendler, M. Ammann, D. J. Donaldson, C. George, *Proc. Natl. Acad. Sci. U.S.A.* **2010**, *107*, 6605.

[21] J. Xia, F. Chen, J. Li, N. Tao, *Nat Nanotechnol* **2009**, *4*, 505.

[22] S. J. Harris, A. M. Weiner, *Annual Review of Physical Chemistry* **1985**, *36*, 31.

[23] A. C. Ferrari, J. Robertson, *Physical review B* **2000**, *61*, 14095.

[24] C. Kohrt, R. Gomer, *Surface Science* **1973**, *40*, 71.

[25] I. Ghouma, M. Jeguirim, L. Limousy, N. Bader, A. Ouederni, S. Bennici, *Materials* **2018**, *11*, 622.

[26] J. Kong, N. R. Franklin, C. Zhou, M. G. Chapline, S. Peng, K. Cho, H. Dai, *Science* **2000**, *287*, 622.

[27] Y. Liu, H. Liu, Y. Chu, Y. Cui, T. Hayasaka, V. Dasaka, L. Nguyen, L. Lin, *Advanced Materials Interfaces* **2018**, *5*, 1701640.

[28] S. Nufer, M. J. Large, A. A. King, S. P. Ogilvie, A. Brunton, A. B. Dalton, *ACS applied materials & interfaces* **2018**, *10*, 21740.

[29] S. S. Varghese, S. Lonkar, K. Singh, S. Swaminathan, A. Abdala, *Sensors and Actuators B: Chemical* **2015**, *218*, 160.

[30] S. Schwartz, W. White, *Solubility Equilibria of the Nitrogen Oxides and Oxyacids in Dilute Aqueous Solution*, Gordon And Breach Science Publishers, **1981**.

[31] A. J. Sweeney, Y. Liu, *Industrial & engineering chemistry research* **2001**, *40*, 2618.

[32] S. Decesari, M. Facchini, E. Matta, M. Mircea, S. Fuzzi, A. Chughtai, D. Smith, *Atmospheric Environment* **2002**, *36*, 1827.

[33] E. Weingartner, H. Burtscher, U. Baltensperger, *Atmospheric Environment* **1997**, *31*, 2311.

[34] A. R. Koh, B. Hwang, K. C. Roh, K. Kim, *Physical Chemistry Chemical Physics* **2014**, *16*, 15146.

[35] S. W. Lee, W. Lee, Y. Hong, G. Lee, D. S. Yoon, *Sensors and Actuators B: Chemical* **2018**, *255*, 1788.

[36] F. Schedin, A. K. Geim, S. V. Morozov, E. W. Hill, P. Blake, M. I. Katsnelson, K. S. Novoselov, *Nat Mater* **2007**, *6*, 652.

[37] J. Li, Y. J. Lu, Q. Ye, M. Cinke, J. Han, M. Meyyappan, *Nano Letters* **2003**, *3*, 929.

[38] H.-B. Lin, J.-S. Shih, *Sensors and Actuators B: Chemical* **2003**, *92*, 243.

[39] F. Yavari, Z. Chen, A. V. Thomas, W. Ren, H.-M. Cheng, N. Koratkar, *Scientific reports* **2011**, *1*, 166.

[40] S. Sharma, M. Madou, *Philos Trans A Math Phys Eng Sci* **2012**, *370*, 2448.

Author contributions

S.N. performed development and fabrication of samples, devices and the gas measurements. C.E. and N.T. analysed the sensing mechanism. P.L. performed the cyclic voltammetry measurements. S.N., M.L, S.O., A.D., C.E. and P.L. were responsible for the preparation of the manuscript. E.M., M.P., R.A. were responsible for the TEM images taken. J.S. was responsible for the collection of the SEM data. W.K.M. and A.M.B. prepared the graphene oxide sample and analysed the XPS data. A.B and A.D. were responsible for the overall direction of the project.

Competing Interest

The authors declare no competing interests.

A gas sensing mechanism based on the present native water layer at ambient conditions is presented using a carbon aerogel structure. NO_2 dissolves in the water layer changing its ionic content which is picked up by the conductive amorphous carbon structure. The high surface area structure is able to detect lowest concentrations of NO_2 at room temperature.

ToC-Figure

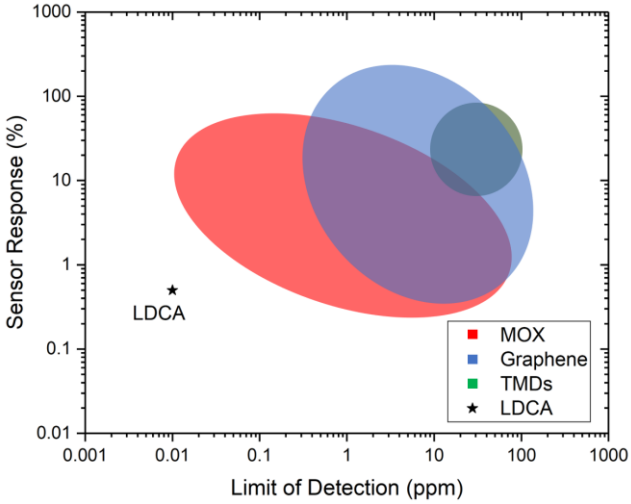

Supporting Information

Exploiting surface water on Carbon Aerogels for ultra-sensitive and selective NO_2 Gas Detection

Sebastian Nufer[1,2,*], Peter J. Lynch[2], Matthew J. Large[2], Sean P. Ogilvie[2], Jonathan P. Salvage[3], Mario Pelaez-Fernandez[4], Edgar Muñoz[5], Raul Arenal[4,6,7], Ana M. Benito[5], Wolfgang K. Maser[5], Nikos Tagmatarchis[8], Chris Ewels[9,*], Adam Brunton[1], Alan B. Dalton[2,*]

1 M-Solv Ltd, Oxonian Park, Langford Locks, Kidlington, Oxford, OX5 1FP, UK, Sebastian.Nufer@m-solv.com
2 University of Sussex, Department of Physics and Astronomy, Brighton, BN1 9RH, UK, A.B.Dalton@sussex.ac.uk
3 University of Brighton, School of Pharmacy and Biomolecular Science, Brighton, BN2

4GJ, UK
4 Instituto de Nanociencia de Aragon, Universidad de Zaragoza, Laboratorio de Microscopias Avanzadas (LMA), 50018 Zaragoza, Spain
5 Instituto de Carboquímica ICB-CSIC, 50018 Zaragoza, Spain
6 Fundacion ARAID, 50018 Zaragoza, Spain
7 Instituto de Ciencias de Materiales de Aragon, CSIC-Universidad de Zaragoza, 50009 Zaragoza, Spain
8 Theoretical and Physical Chemistry Institute, National Hellenic Research Foundation, 48 Vassileos Constantinou Avenue, 11635 Athens, Greece
9 Institute des Matériaux Jean Rouxel (IMN), CNRS UMR6502 / Université de Nantes, Nantes, 44322, France, Chris.Ewels@cnrs-imn.fr

Device Fabrication

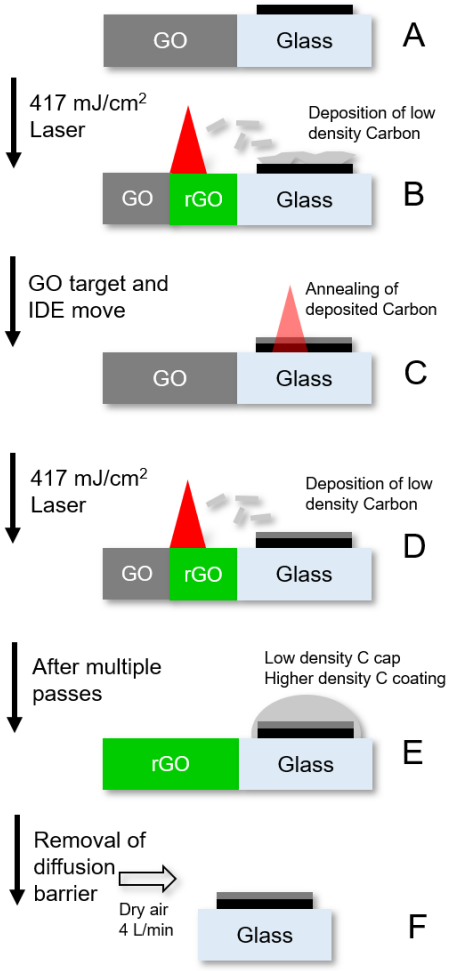

Fig. S1. Detailed fabrication schematic. (A) GO and IDEs are placed level next to each other. (B) the GO is irradiated using a IR laser synthesising carbon clusters which diffuse on to the IDEs – the GO becomes rGO at the same time. (C) GO and IDEs move an increment before laser starts irradiating the IDEs, annealing the already deposited carbon on the IDEs. (D) laser beam continues on GO depositing more carbon clusters on the already existing annealed carbon. (E) a complete annealed active film is synthesized on the IDEs and covered in carbon foam, which is not annealed and (F) carbon diffusion barrier is blown of using dry air releasing the active layer.

Graphene Oxide synthesis

Graphite oxide was prepared from graphite powder (Sigma Aldrich, Ref. 332461) using a modified Hummers' method as described elsewhere.[1,2] In brief, 170 mL of concentrated H_2SO_4 was added to a mixture of graphite flakes (5.0 g) and $NaNO_3$ (3.75 g). The mixture was vigorously stirred for 30 minutes in an ice bath. $KMnO_4$ (25 mg) was slowly added while stirring for another 30 minutes. The reaction was then warmed up to 35 ºC and stirred overnight. Subsequently, distilled water (250 ml) and 30% H_20_2 (20 mL) were slowly added in sequence. The mixture was stirred for 1 hour, filtered and washed repeatedly with 400 mL

of HCl:H_2O (1:10), and dried in air, thus yielding graphite oxide. Finally, the resulting graphite oxide was dispersed in water at a concentration of 2 mg/mL and bath sonicated for 2 hours. This led to a brown-coloured dispersion of exfoliated graphene oxide flakes.

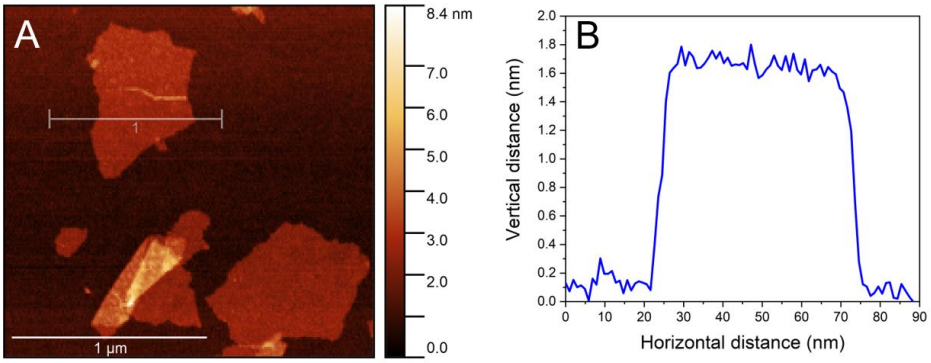

Fig. S2. Characterisation of synthesized GO flakes. (A) AFM image of GO flakes produced by the modified Hummer's method. (B) Height profile of flake showing a height of 1.8 nm of the flake.

Note S1. GO analysis. Fig. S2 shows an AFM measurement of the GO flakes and the *associated* height profile. Flakes are in the micrometre regime in terms of size and are 1.8 nm thick showing single layer graphene oxide. The AFM measurement was taken using a Bruker Icon with a TESPA-V2 antimony doped silicon tip, with 1024 samples per line at a frequency of 0.5 Hz.

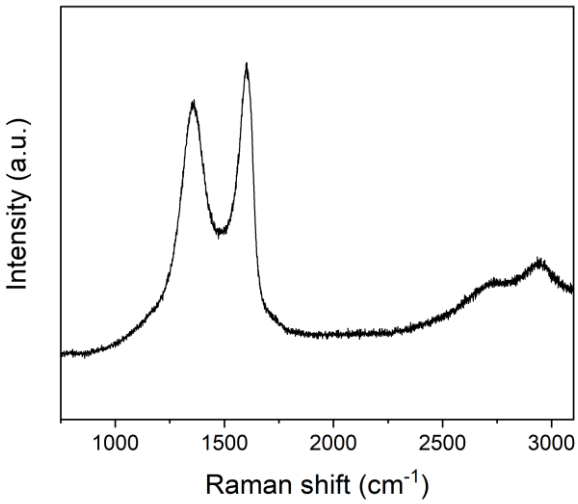

Fig. S3. Raman spectrum of synthesized GO.

Note S2: Raman analysis GO. Fig. S3 shows the Raman spectrum of the synthesized GO with the characteristic D and G peak around 1300 and 1600 cm^{-1}. The Raman spectrum was taken using a 532 nm laser at 5 mW for a duration of 20 sec and 10 accumulation repetitions.

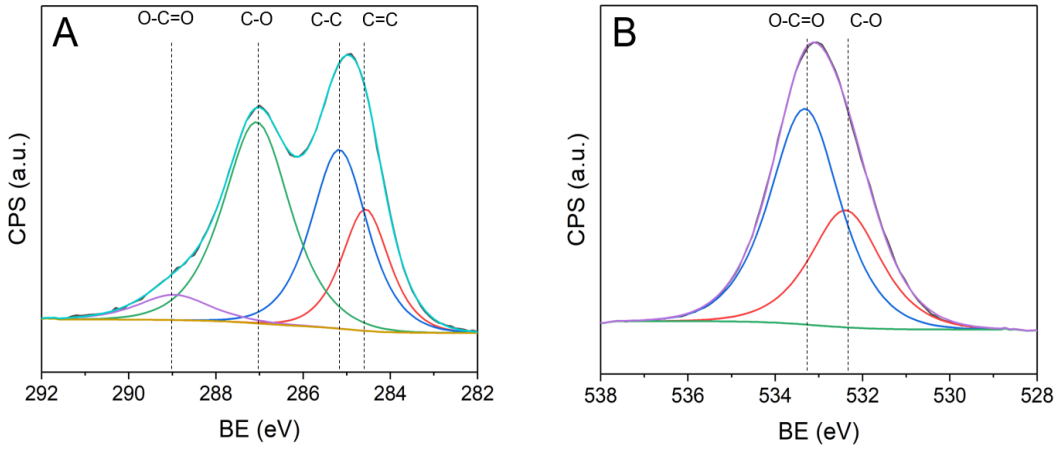

Fig. S4. XPS spectra of GO. (A) Deconvoluted XPS C1 peak spectrum of GO. (B) Deconvoluted XPS Oxygen peak spectrum of GO.

Note S3. XPS analysis of GO. XPS of the GO C1s appears in the range from 282 to 292 eV, and was deconvoluted using CASA XPS software. The XPS peaks were fitted to GL(70) Voigt lineshape (a combination of 70% Gaussian and 30% Lorentzian character), after performing a Shirley background subtraction. In the fitting procedure, the FWHM (full width at half maximum) values were fixed at a maximum limit of 1.6 eV for all the peaks except the peaks appearing at the higher energy region that tend to be much broader. Asymmetry for the Sp2 carbon peak was defined as a function LA(α, β, m), where α=0.4 and β=0.38 describe the spread of the tail on each side of the Lorentzian component and the parameter m=70 specifies the width of the Gaussian used to convolute the Lorentzian curve. The C1s region of GO XPS spectrum was deconvoluted into four peaks located at binding energies (BE) of 284.6 (Sp2 C=C species), 285.2 carbon atoms in Sp3 structures), 287 (C-O, alcohol/ether/epoxy groups) and 288.9 eV (COOH, carboxylic acid/ester groups). Deconvolution of O1s spectra yields 2 main peaks (FWHM value of 1.8 eV each peak) around 532.4 and 533.3 eV assigned to C-O (epoxy, phenol groups) and O-C=O (carboxylic, ester groups).

XPS comparison GO, diffusion layer aerogel and active aerogel

System	C/O ratio
GO	3.4
aerogel – diffusion layer	5.3
aerogel- active layer	5.0

Table S1. C/O ratio GO, aerogel diffusion barrier and aerogel active layer extracted from XPS spectrum.

	Sp2 C=C	Sp3	C-O	COOH
Peak position	284.5 ± 0.3	285.5 ± 0.3	286.4 ± 0.3	290 ± 0.3
GO	18.6	32.4	43.2	5.8
aerogel – diffusion barrier	22.5	50.4	21.7	5.4
aerogel – active layer	62.2	19.5	12.4	5.8

Table S2. C1-peak % content deconvolution of GO % content, aerogel diffusion barrier and aerogel active layer.

	C=O	C-O	O-C=O	Water
Peak position	531.3	532.3 ± 0.2	533.3 ± 0.2	536.6 ± 0.1
GO	-	35.3	64.7	-
aerogel – diffusion barrier	-	34.4	62	3.6

aerogel – active layer	24.6	37.4	37.21	0.8

Table S3. O1-peak % content deconvolution GO, aerogel diffusion barrier, aerogel active layer.

Note S4. XPS analysis of different states of aerogel during fabrication. The % content of various oxygen functional groups are shown in Supplementary Table S1-3. These values show the characteristics before laser irradiation (GO), after the first laser irradiation (aerogel – diffusion layer) and after the second laser irradiation (aerogel-active layer). The carbon content increases after the first laser irradiation process due the removal of oxygen functional groups.[3,4] The second laser irradiation process changes the oxygen content in the aerogel slightly. The laser irradiation increases the carbon sp^2 content significantly, lowering the carbon sp^3 content, between individual steps. The presence of sp^2 hybridized carbons enhances the conductivity in the material. Oxygen functional groups are removed from the aerogel through the laser irradiation, especially C-O species. There is water bonded to the carbon after the first laser irradiation, which is partly removed in the second irradiation step. The water is added to the aerogel from the ambient environment in which the laser process takes place.

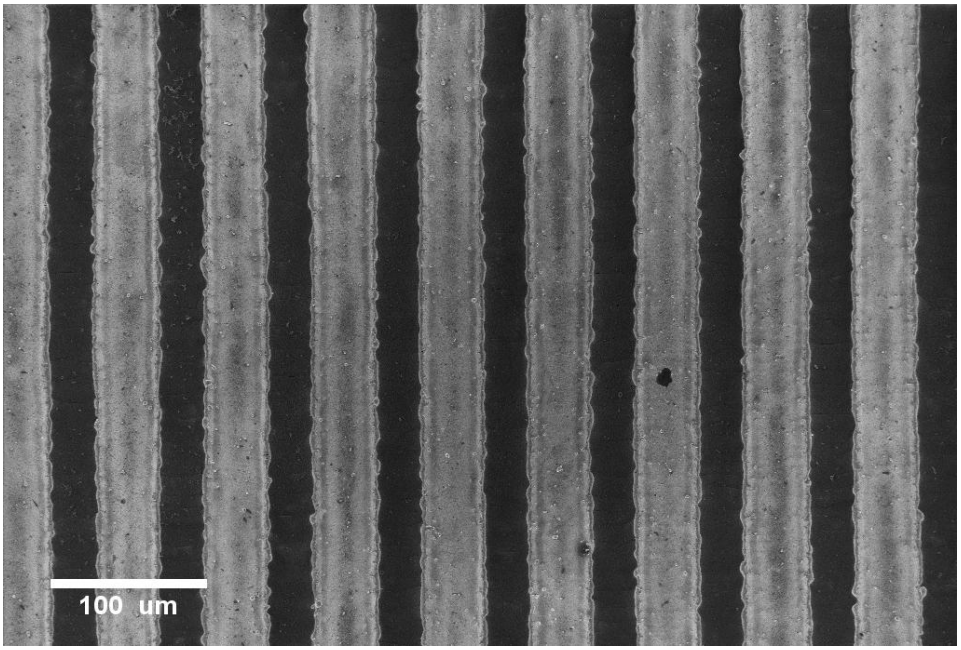

Fig. S5. SEM image of laser ablated IDEs.

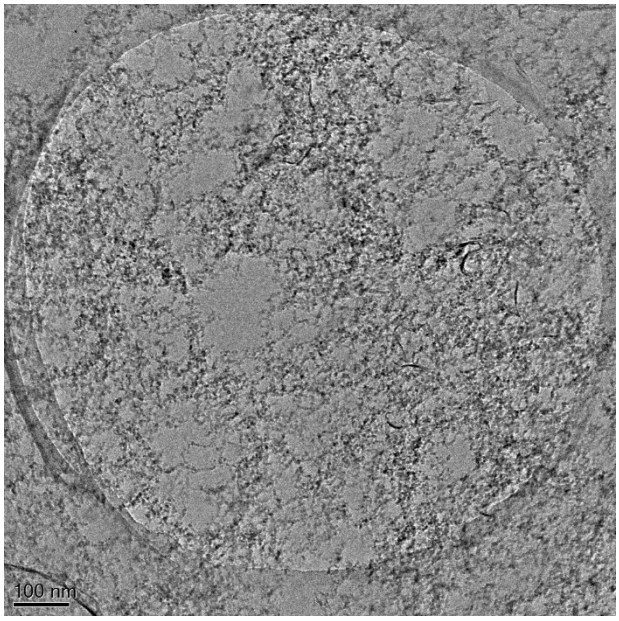

Fig. S6. TEM image of aerogel at lower magnification showing the fractal assembly character of the diffusion limited aggregation formation process.

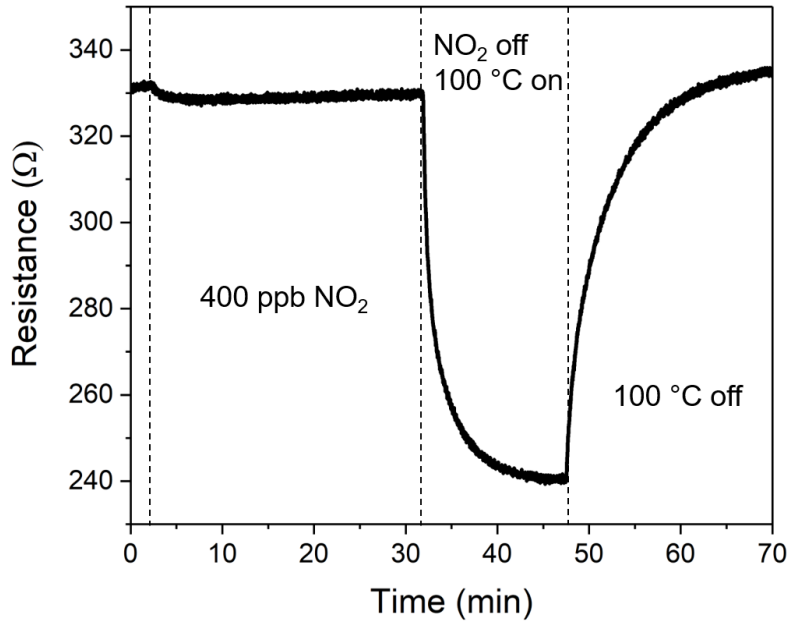

Fig. S7. After NO_2 exposure ends, the device resistance drops, however the aerogel does not recover to the baseline resistance on its own. A heating step is applied to aid desorption the analyte and recovery of the baseline device resistance.

Note S5. BET calculation. Owing to the increasing sensitivity (indicated by the value of S_{max}) with humidity, we use the BET isotherm[5] to evaluate the thickness of the adsorbed water layer on the LDCA as a function of humidity;

$$\frac{t}{t_{mono}} = \frac{\beta \mathrm{H}}{(1-\mathrm{H})(1-(1-\beta)\mathrm{H})}$$

where t is the estimated thickness of the water layer; t_{mono} is the thickness of a monolayer of adsorbed water ($t_{mono} = 0.25 \pm 0.05$ nm [6]); $\beta \approx \exp\left[\left(\Delta H_d - \Delta H_{vap}\right)/RT\right]$ where ΔH_d is the enthalpy of desorption of water from LCDA; $\Delta H_{vap} = 40650\ \mathrm{J/mol}$ is the enthalpy of vaporisation of water; $R = 8.314\ \mathrm{J/mol \cdot K}$ is the ideal gas constant; T is the absolute temperature; $H = P/P_0$ is the fractional relative humidity, where P and P_0 are the partial pressure and saturation partial pressure of water in the atmosphere, respectively.

By treating

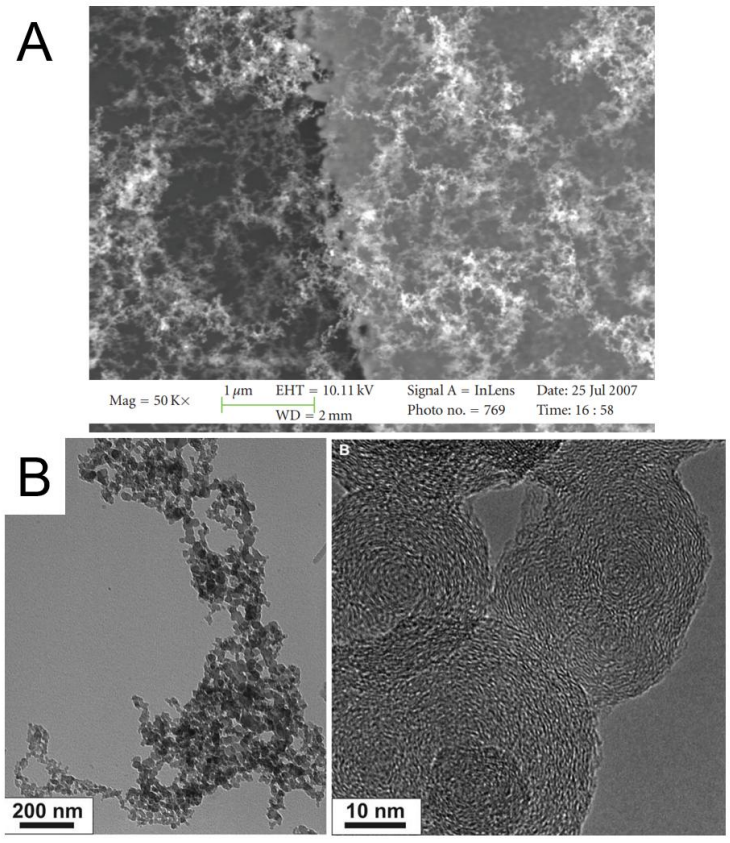

atistic $|1 - R^2|$ of

Fig. S8. (A) SEM image of propane flame soot [reproduced with permission from Reference [9]]. (B) TEM images of diesel soot [reproduced with permissiom from Ref [10]].

the values for S_{max} and t (as functions of H), we arrive at a direct correlation between the

device sensitivity and thickness of the adsorbed water layer. This is illustrated in **Figure 4A**,

where the optimised value for $\Delta H_d = 50000 \pm 600$ J/mol.

The value is comparable to the water adsorption enthalpy found for graphene oxide (73116

J/mol [7]) and is within the broad range reported for various carbons (10,000-80,000 J/mol [8]).

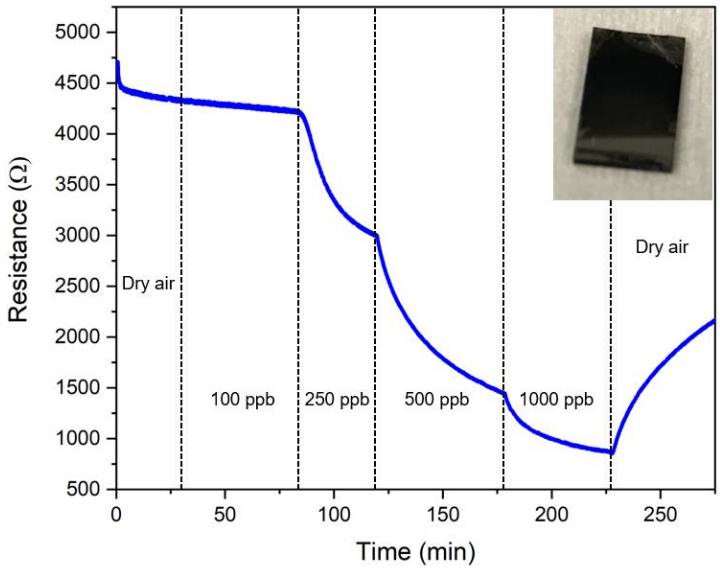

Fig. S9. Resistance measurement of propane soot when exposed to various concentrations of NO_2 in dry air. Inset shows soot deposited with a lighter onto interdigitated electrodes.

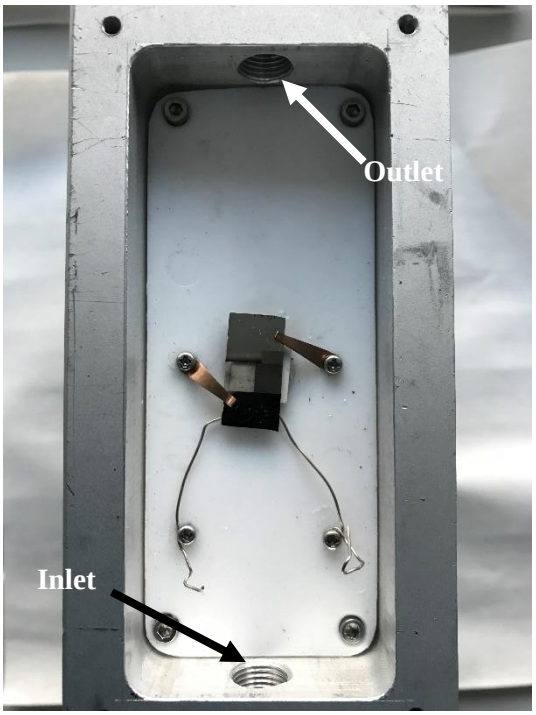

Fig. S10. Gas measurement chamber with device clamped on to ceramic hotplate. Inlet and outlet of the chamber are marked. Electrical connections through mechanical clamps.

References:

[1] W. S. Hummers Jr, R. E. Offeman, *Journal of the American Chemical Society* **1958**, *80*, 1339.

[2] C. Vallés, J. D. Núñez, A. M. Benito, W. K. Maser, *Carbon* **2012**, *50*, 835.

[3] E. Kymakis, C. Petridis, T. D. Anthopoulos, E. Stratakis, *IEEE Journal of Selected Topics in Quantum Electronics* **2014**, *20*, 106.

[4] R. Trusovas, K. Ratautas, G. Ravciukaitis, J. Barkauskas, I. Stankevivciene, G. Niaura, R. Mavzeikiene, *Carbon* **2013**, *52*, 574.

[5] E. Wensink, A. Hoffmann, M. Apol, H. Berendsen, *Langmuir* **2000**, *16*, 7392.

[6] A. Opitz, M. Scherge, S.-U. Ahmed, J. Schaefer, *Journal of applied physics* **2007**, *101*, 064310.

[7] B. Lian, S. De Luca, Y. You, S. Alwarappan, M. Yoshimura, V. Sahajwalla, S. Smith, G. Leslie, R. Joshi, *Chemical science* **2018**, *9*, 5106.

[8] S. Furmaniak, P. A. Gauden, A. P. Terzyk, G. Rychlicki, *Advances in Colloid and Interface Science* **2008**, *137*, 82.

[9] D. Lutic, J. Pagels, R. Bjorklund, P. Josza, J. H. Visser, A. W. Grant, M. L. Johansson, J. Paaso, P.-E. Fägerman, M. Sanati, others, *Journal of sensors* **2010**, *2010*, 6.

[10] H. H. Pawlyta Mirosława, *Annales Societatis Geologorum Poloniae* **2016**, *86*, 2.